CASTOR: Normal-Mode Analysis of Resistive MHD Plasmas

W. Kerner,* J. P. Goedbloed,† G. T. A. Huysmans,* S. Poedts,† and E. Schwarz‡

*JET Joint Undertaking, Abingdon, Oxfordshire OX143EA, United Kingdom;
†FOM Institute for Plasma Physics Rijnhuizen, Nieuwegein, The Netherlands;
‡MPI für Plasmaphysik, EURATOM Ass. D-85748 Garching, Germany
E-mail: Wolfgang.kerner@jet.uk

The CASTOR (complex Alfvén spectrum of toroidal plasmas) code computes the entire spectrum of normal-modes in resistive MHD for general tokamak configurations. The applied Galerkin method, in conjunction with a Fourier finite-element discretisation, leads to a large scale eigenvalue problem $\mathbf{A}\underline{x} = \lambda \mathbf{B}\underline{x}$, where $\mathbf{A}$ is a nonself-adjoint matrix.   © 1998 Academic Press

Key Words: magnetohydrodynamics; resistive; toroidal; spectrum.

I. INTRODUCTION

The gross macroscopic properties of a fusion oriented device, such as JET, concerning equilibrium, stability, and transport are of special interest. The magnetohydrodynamic theory (MHD) combining fluid equations and Maxwell's equations describes this macroscopic behaviour. The role of ideal MHD in magnetic fusion is in the first place to discover magnetic geometries with favourable equilibrium and stability properties. Fast global ideal instabilities have to be avoided. Nonideal effects allow development of slower and weaker instabilities leading to enhanced transport and violent disruptions. Since MHD characteristics are observed in most experimental phenomena, a detailed knowledge about the stable and unstable MHD solutions is required not solely stability limits. The theory of equilibria and linearised motion around an equilibrium configuration has, therefore, been in the centre of theoretical investigations over the years. The most complete picture is obtained by means of a normal-mode analysis, which yields the various temporal and spatial scales inherent in the specific MHD model used. The MHD spectrum, especially the Alfvén continuum, has played an important role in the understanding of instabilities and wave heating via resonant absorption.

In this paper we adopt the picture of a tokamak equilibrium given by ideal MHD with isotropic pressure, i.e. by $\underline{J} \times \underline{B} = \nabla p$, and subjected to dissipative perturbations. This

271

viewpoint is justified by a hierarchy of time scales. Since finite conductivity causes the plasma to break away from the magnetic field and prompts unfavourable changes of the magnetic topology with large and small islands leading to ergodic fields, the resistive perturbations have to be studied even for large but finite conductivity. The approach incorporates a flux coordinate system based on the specific equilibrium, in order to model the Alfvén branch accurately. Clearly, the Alfvén branch of the spectrum is the most relevant part for magnetic confinement. The name "CASTOR," i.e. complex Alfvén spectrum of toroidal plasmas, given to the new normal-mode code reflects this viewpoint.

The finite-element method provides a flexible and highly accurate numerical approximation. In dissipative MHD this prompts a nonvariational form with general non-Hermitian matrices and complex eigenvalues. The discretisation has then to be chosen carefully in order to avoid spurious nonphysical oscillatory solutions. A "pollution-free" approximation has been established. Powerful algorithms exist for the solution of the linear eigenvalue problem. The specific difficulty for us is given by the large dimensions of the system which indicates that iterative methods, such as vector iteration, preserving the sparseness of the matrices are preferable. Such a scheme can be extended to a shifted Lanczos algorithm for mapping out specific parts of the spectrum. The storage of large-scale matrices with $(1–10)\times10^6$ nonzero elements can easily be arranged if external storage is addressed. The linear algebra algorithms involved in the eigenproblem can be tailored to reach peak performance by fully utilising vectorisation and parallelism as discussed in Refs. [1, 2].

The paper is organised as follows: The physical model appropriate to simulating the dissipative plasma behaviour is presented in Section II. The tokamak equilibria considered are described by ideal MHD and define specific nonorthogonal flux coordinates. Section III contains the numerical method. The resistive MHD equations are solved in their weak form by applying the finite-element method. This leads to a large-scale complex eigenvalue problem. The derivation of the corresponding matrix elements is outlined in Section IV. Applications displaying the accuracy and efficiency of the numerical scheme are presented in Section V. Finally, Section VI contains the discussion and conclusion. The matrix elements are listed in Appendix A and the equilibrium quantities in Appendix B. Details of the finite elements employed are given in Appendix C.

II. PHYSICAL MODEL

The single-fluid MHD equations in normalised, dimensionless form read:
continuity,

$$\frac{\partial \rho}{\partial t} + \nabla(\rho \underline{v}) = 0; \tag{2.1}$$

momentum,

$$m\rho\left(\frac{\partial}{\partial t} + \underline{v} \cdot \nabla\right)\underline{v} = -\nabla p + \underline{j} \times \underline{B}; \tag{2.2}$$

energy,

$$\rho\left(\frac{\partial}{\partial t} + \underline{v} \cdot \nabla\right)T = (\gamma - 1)[-p\nabla \cdot \underline{v} - \nabla \cdot \underline{q} + \eta j^2] \tag{2.3}$$

with $\gamma = 5/3$ the ratio of specific heats and Ohm's law (in simplified form),

$$E + \underline{v} \times \underline{B} = \eta \underline{j}, \tag{2.4}$$

where $\underline{q}$ denotes the heat flux and η is the resistivity. This model relates the density ρ, velocity $\underline{v}$, scalar pressure p, temperature T, the magnetic (electric) field $\underline{B}(\underline{E})$, and the current $\underline{j}$. In addition, we have

Maxwell,

$$\frac{\partial \underline{B}}{\partial t} = -\nabla \times \underline{E}, \tag{2.5}$$

$$\underline{j} = \nabla \times \underline{B}, \tag{2.6}$$

$$\nabla \cdot \underline{B} = 0; \tag{2.7}$$

ideal gas law,

$$p = \rho T. \tag{2.8}$$

The basic uncertainties in this model with respect to modelling plasmas in a fusion reactor are given by the omission of kinetic effects in the pressure tensor, i.e. $\mathbf{\Pi} = 0$, and by the neglect of the electron response in Ohm's law. This formulation based on density and temperature as variables is well suited for the study of thermal instabilities with nonzero parallel and perpendicular heat conductivities in the heat flux (see conclusions). For the discussion of the numerical scheme the heat conductivity is set to zero throughout this paper.

The standard model applied to equilibrium and stability begins with a static ($\underline{v} \equiv 0$) steady-state ($\partial/\partial t = 0$) equilibrium which reduces to

$$(\nabla \times \underline{B}_0) \times \underline{B}_0 = \nabla p_0,$$
$$\nabla \cdot \underline{B}_0 = 0. \tag{2.9}$$

The condition that the magnetic field be divergence-free is incorporated in the representation

$$\underline{B}_0 = \nabla \phi \times \nabla \psi + F(\psi) \nabla \phi, \tag{2.10}$$

where ψ denotes the poloidal flux and F is the poloidal current profile. The equilibrium geometry is presented in Fig. 1. Cylindrical coordinates R, ϕ, z are used and axisymmetry implies that the equilibrium quantities do not depend on ϕ. Force balance leads to the Grad–Shafranov equation for ψ defining a nested set of closed magnetic surfaces. The plasma behaviour is quite anisotropic with respect to the directions parallel and perpendicular to $\underline{B}_0$. Therefore it is essential to utilise ψ as a radial coordinate. Such a flux coordinate system ψ, θ, ϕ is characterised by its Jacobian,

$$J^{-1} = \nabla \psi \times \nabla \theta \cdot \nabla \phi, \tag{2.11}$$

where θ denotes an angle in the poloidal direction, e.g. a polar angle. A straight field line coordinate system ψ, χ, ϕ is characterised by a constant ratio,

$$B_0^\phi / B_0^\chi = q(\psi), \tag{2.12}$$

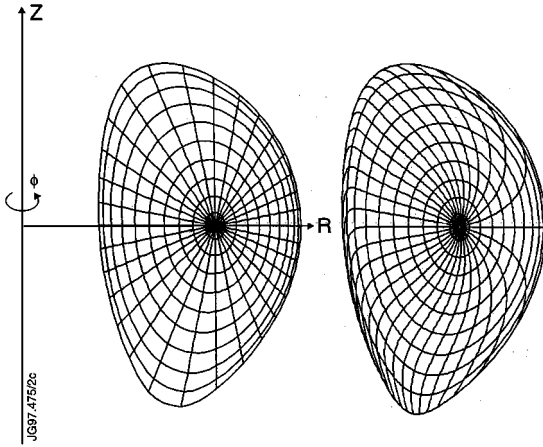**FIG. 1.** The poloidal cross section of a typical JET equilibrium displaying the closed contours of equal flux, $s = \sqrt{\psi/\psi_s}$; R, ϕ, Z, denote cylindrical coordinates. The vacuum region outside the last closed flux surface extends up to an arbitraily shaped wall (not shown): (a) lines of constant polar angle (of the s, θ, ϕ coordinates). (b) lines of constant angle χ (of the straight field lines coordinates s, χ, ϕ, which is constructed by integration on s = ct).

where q denotes the safety factor. Then the operator $\underline{B}_0 \cdot \nabla$ has the representation

$$JB_0 \cdot \nabla = \left(q(\psi)\frac{\partial}{\partial\phi} + \frac{\partial}{\partial\chi} \right) = i(nq(\psi) + m) \tag{2.13}$$

with n and m denoting the toroidal and poloidal wave numbers. Consequently the ψ, χ, ϕ coordinate system is uniquely defined by the choice

$$J = \frac{R^2 q(\psi)}{F(\psi)}. \tag{2.14}$$

The theory of linearised perturbations adopts an expansion around such an equilibrium and linearises the equations. This is then the place where dissipation is taken into account. The justification for this procedure is given by estimating the time scales of interest. In the limit of small resistivity η the equilibrium profile evolution, proportional to η, is very slow, whereas the perturbations grow on a faster time scale typically of the order of

$$t \sim \eta^{3/5} \quad \text{or} \quad \eta^{1/3}, \tag{2.15a}$$

where the resistive layer scaling is

$$r_L \sim \eta^{2/5} \quad \text{or} \quad \eta^{1/3} \tag{2.15b}$$

is quite small.

The relevant stable waves such as Alfvén waves experience only small damping. Thus we can adopt the standard model.

All quantities are expanded around the equilibrium in the form

$$y(\underline{r}, t) = y_0(\underline{r}) + e^{\lambda t}y(\underline{r}), \tag{2.16}$$

where we keep the subscript 0, but we omit the subscript 1 for the perturbations y.

Here, λ is the eigenvalue. The imaginary part of λ corresponds to oscillatory behaviour, while a negative real part yields damping and a positive real part yields an exponentially growing instability. As it will become apparent that the correct treatment of the magnetic field perturbation under the influence of finite resistivity is essential, we will focus on the extension of the scheme to fully two-dimensional equilibria with only resistivity taken into account. No perturbation of the resisitivity is included here.

With resistivity η_0 the equations for the perturbed quantities ρ, $\underline{u}$ (perturbed velocity), T, and $\underline{b}$ read

$$\lambda \rho = -\nabla \cdot (\rho_0 \underline{u}), \tag{2.17a}$$

$$\lambda \rho_0 \underline{u} = -\nabla(\rho_0 T + T_0 \rho) + (\nabla \times \underline{B}_0) \times \underline{b} + (\nabla \times \underline{b}) \times \underline{B}_0 \tag{2.17b}$$

$$\lambda \rho_0 T = -\rho_0 \underline{u} \cdot \nabla T_0 - (\gamma - 1)\rho_0 T_0 \nabla \cdot \underline{u} + (\gamma - 1)[2\eta_0 \nabla \times \underline{B}_0 \cdot \nabla \times \underline{b}], \tag{2.17c}$$

$$\lambda \underline{b} = \nabla \times (\underline{u} \times \underline{B}_0 - \eta_0 \nabla \times \underline{b}). \tag{2.17d}$$

The dissipated energy in (2.17c) can be neglected, as is done usually.

The condition $\nabla \cdot \underline{b} = 0$ is satisfied if $\underline{B}_0$ is divergence-free. The vector potential is introduced by

$$\underline{b} = \nabla \times \underline{a} \quad \text{and} \quad \underline{E} = -\lambda \underline{a}, \tag{2.18}$$

where the scalar potential is set equal to zero.

The induction equation now reads

$$\lambda \underline{a} = \underline{u} \times \underline{B}_0 - \eta_0 \nabla \times \nabla \times \underline{a} \tag{2.17e}$$

and $\underline{b}$ is replaced by $\nabla \times \underline{a}$ in (2.17b). It will be shown in Section III that this formulation is well suited for the numerical approximation of the entire spectrum. Thus the system (2.17a), (2.17b), (2.17c), and (2.17e) is the basis of the CASTOR code.

The boundary conditions at a perfectly conducting wall are

$$\underline{n} \cdot \underline{u} = 0, \quad \underline{n} \cdot \underline{b} = 0, \quad \underline{n} \times \underline{E} = 0, \tag{2.19}$$

where $\underline{n}$ is the outward pointing normal vector.

When a plasma–vacuum–wall system is considered, the perturbed vacuum field can be expressed by a potential,

$$\underline{b}_v = \nabla \phi_v. \tag{2.20}$$

Maxwell equations (2.6), (2.7) then imply

$$\nabla^2 \phi_v = 0. \tag{2.21}$$

The ideal MHD ($\eta \equiv 0$) boundary conditions indicate that the normal magnetic field and the total pressure $\pi = p + 1/2\underline{B}^2$ are continuous at the perturbed plasma–vacuum interface and $\underline{n} \cdot \underline{b}_v = 0$ at the wall. In the case where the equilibrium magnetic field is continuous across the plasma boundary the pressure p_0 falls to zero at the boundary. Then the boundary conditions assume the form

$$\underline{b} \cdot \underline{n} = \underline{b}_v \cdot \underline{n} \tag{2.22}$$

$$\pi_1 = P + \underline{B}_0 \cdot \underline{b} = \underline{B}_{0v} \cdot \underline{b}_V, \tag{2.23}$$

where the perturbed pressure is given by $P = \rho_0 T + \rho T_0$.

For finite resistivity at the boundary surface currents are no longer allowed in the plasma perturbations and, therefore, all three components of the perturbed magnetic field are continuous. This gives rise to two additional resistive boundary conditions $\underline{B} \times \underline{n} = \underline{B}_v \times \underline{n}$, which for equilibria with zero surface currents implies

$$\underline{n} \times \underline{b} = n \times \underline{b}_v. \tag{2.24}$$

These conditions are incorporated in the surface terms which occur by constructing the weak form in Section IV.5.

At the magnetic axis the boundary conditions are given by the regularity condition on axis.

III. NUMERICAL METHOD

The method adopted for numerical solution is subjected to two different requirements. First, it should apply to general configurations in solar and stellar plasmas as well as to fusion-relevant tokamak configurations. Second, it should be easily extended to include various forms of dissipation. Such requirements exclude elimination of specific components of the perturbation and prompt a general solution of the system (2.17). Hence we are prepared to solve large-scale systems. Thereby, full use can be made of the theory and of the algorithms available in linear algebra for solving the eigenvalue problem (see Kerner [1]). It has been shown previously that the corresponding systems can be solved for efficiently and accurately in plasmas with cylindrical symmetry [3].

It is recalled that the ideal MHD spectrum typically splits into three branches, namely the fast magneto-acoustic waves, the Alfvén waves, and in the small pressure limit the sound waves with a large ratio of the largest to smallest eigenvalue. This indicates that special care is necessary to ensure correct and accurate numerical representation of the entire spectrum.

The framework for numerical solution of the dissipative MHD equations is given by the finite-element method.

1. *Discretisation*

For tokamak systems it is advantageous to apply a Fourier finite-element discretisation in the flux coordinate system s, χ, ϕ, adopted to the specific axisymmetric equilibrium considered with

$$s = \sqrt{\psi/\psi_s}, \quad 0 \leq s \leq 1, \tag{3.1}$$

and

$$f(s) = \frac{d\psi}{ds} = 2s\psi_s \tag{3.2}$$

with ψ_s the flux on the boundary.

The Jacobian is

$$J = f(s)R^2 q(s)/F(s). \tag{3.3}$$

The perturbations introduced in (2.16) are represented by the ansatz

$$\underline{y}(\underline{r}) = \exp(in\phi) \sum_{m=-\infty}^{m=\infty} \underline{y}_m(s) \exp(im\chi). \tag{3.4}$$

The radial dependence of $\underline{y}$ is expressed by a linear combination of local expansion or shape functions $h_j(s)$:

$$y_m(s) = \sum_{j=1}^{N_s} (x_m)_j h_j(s). \tag{3.5}$$

The expansion coefficients $(x_m)_j$ are determined numerically, together with the eigenvalue and they form the eigenvector.

The normal-mode problem exhibits very different spatial and temporal scales, as manifested in the different branches of the spectrum and in the very localised, almost singular, resistive instabilities. Special care is therefore required in choosing the appropriate numerical approximation for the different components of the perturbations. Optimal numerical approximation of the entire computed spectrum is obtained if the discretisation is chosen to satisfy two constraints in every point,

$$\nabla \cdot \underline{u} = 0 \tag{3.6a}$$

$$\nabla \cdot \underline{b} = 0. \tag{3.6b}$$

When unphysical coupling between the fast magnetosonic and the Alfvén waves occurs the Alfvén spectrum is highly distorted numerically. In toroidal systems the fast modes are suppressed in leading order in inverse aspect ratio if the perturbation satisfies

$$\nabla \cdot (\underline{u}_\perp/R^2) = 0. \tag{3.7}$$

This implies that pure Alfvén waves are represented correctly only if the discretisation satisfies condition (3.7) exactly, independent of the mesh size.

In ideal MHD the linearised system can be cast into a variational problem for the energy in the Lagrangian displacement ξ, which through $\underline{u} = \partial\xi/\partial t$ corresponds to the velocity. This approach was followed in the development of the ideal MHD toroidal stability codes ERATO [4] and PEST [5]. Uniform convergence of the entire computed spectrum towards the correct spectrum, i.e. good convergence for every eigenvalue, is achieved when the discretisation satisfies constraint (3.7). Otherwise, "pollution" is found where a specific eigenvalue converges by increased resolution, but at the same time new incorrect ("polluted") eigenvalues are introduced. A comprehensive discussion of this numerical phenomenon is given by Gruber and Rappaz in Ref. [6]. Two components of $\underline{u}$ can be chosen to put the perpendicular into the form

$$\nabla \cdot (\underline{u}_\perp/R^2) = \frac{1}{J}\left(\frac{\partial u_1}{\partial s} + mu_2\right). \tag{3.8}$$

Thus the constraint (3.7) implies that the basic functions for u_1, called H, are one order higher in s than those of u_2 and u_3 called h:
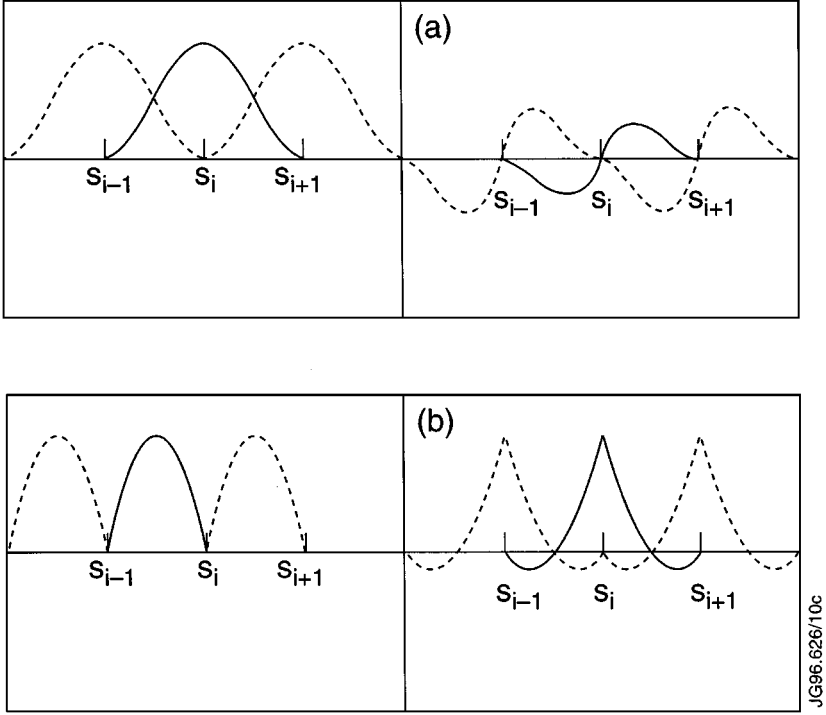
$$\partial H/\partial s = h. \tag{3.9}$$

FIG. 2. Finite elements: (a) cubic Hermite and (b) quadratic expansion functions. The solid curves represent the elements associated with the points s_j and the dashed curves, the neighbouring elements.

This corresponds to a "staggered" mesh used in finite differences. It is sufficient that $H \in C^0$; i.e., the derivatives need not be continuous.

The third component of the velocity is chosen to yield a good numerical approximation of the sound waves. It is emphasised that the conditions (3.6a) and (3.7) constitute constraints for the numerical scheme. The plasma is treated as a compressible medium.

Dissipative MHD yields a nonvariational problem. In order to obtain an equally good numerical approximation higher-order elements H are required for the normal component b_ψ. It is found that these functions have to be in C^1, i.e. have to have continuous derivatives. Cubic Hermite elements are thus used for H and quadratic elements for h. In each case two orthogonal functions define a complete set. The cubic Hermitian elements, together with the quadratic elements are plotted in Fig. 2 and listed explicitly in Appendix C. This choice allows satisfying the condition $\nabla \cdot \underline{b} = 0$ up to machine accuracy. This constraint is, of course, a physical condition.

2. *Approximation of b*

An obvious choice for enforcing the condition $\nabla \cdot \underline{b} = 0$ is to eliminate one component. In Ref. [3] it was shown that eliminating the b_θ component

$$b_\theta = -\frac{r}{im}\left(\frac{1}{r}\frac{\partial}{\partial r}(rb_r) + ikb_z\right) \quad \text{for } m \neq 0 \tag{3.10}$$

yields a pollution-free numerical approximation to the entire spectrum as demonstrated in Fig. 2 of Ref. [3]. In the toroidal system the different Fourier components in the expansion (3.5) couple, including the $m = 0$ component, making the elimination (3.10) impossible. It was found that the elimination of b_ϕ leads to a numerically unstable scheme, since for unstable modes and Alfvén waves b_ϕ is very small but is replaced by two large components which almost cancel each other. This leads to numerical difficulties and should therefore not be done!

To avoid different schemes for $m \neq 0$ and $m = 0$, all three components of the perturbed magnetic field have to be retained. This now leads to a numerical system with additional dimension of $2\,N_s$ for each Fourier component (with N_s the number of finite elements). Therefore, additional $2\,N_sM$ modes occur in the numerically approximated spectrum. Among well-approximated eigen-solutions we find, in addition, spurious modes which are due to nonzero values of $\nabla \cdot b$. Although $\nabla \cdot b$ vanishes analytically,

$$\nabla \cdot \frac{\partial b}{\partial t} = \lambda \nabla \cdot b = -\nabla \cdot \nabla \times E = 0; \tag{3.11}$$

for nonzero eigenvalue ($\lambda \neq 0$) this is not guaranteed numerically for finite resistivity. The cubic Hermite shape functions have continuous derivatives across different elements, $H \in C^1$, but the quadratic ones do not, $h \in C^0$. Finite resistivity in the induction equation leads to radial derivatives of the poloidal and toroidal components of $\underline{b}$, which are expanded in quadratic finite elements. The jump in these terms yields spurious eigenvalues, which are consequently linked to jumps in $\nabla \cdot b$; i.e., $\nabla \cdot \underline{b}; \neq 0$ across different elements. We have not found a simple way to eliminate these jumps. A remedy is found by expanding all three components of $\underline{b}$ in cubic elements $H \in C^1$. Then $\nabla \cdot \underline{b} = 0$ is satisfied also numerically. However, in the limit of $\eta_0 \to 0$ this scheme does not match well the discretisation used for the ideal system ($\eta_0 = 0$).

An accurate numerical solution is produced when the perturbed magnetic field is expressed by a vector potential as introduced in Eq. (2.18), and the induction equation as given by (2.17e). The proper discretisation satisfying the constraints on the numerical method, Eqs. (3.6a), (3.6b), and (3.7), yields an expansion in cubic elements for u_1 (radial velocity component), a_2 (poloidal component of the vector potential), and a_3 (toroidal component of the vector potential), i.e. $u_1, a_2, a_3 \in C^1$, and in quadratic elements for u_2, u_3 and a_1 (normal component) $\in C^0$ as well as for ρ and T.

The weak form yields radial derivatives on a_2 and a_3 only, but not on a_1. The divergence equation (3.11) yields

$$\lambda \nabla \cdot \underline{b} = 0, \tag{3.12a}$$

with the consequence that for nonzero eigenvalues $\nabla \cdot \underline{b}$ is zero up to the machine accuracy.

The additional spurious modes now lie on the origin of the complex plane

$$|\lambda(\text{spurious})| < 10^{-12}. \tag{3.12c}$$

This has, indeed, been verified by many numerical runs.

It should be added that the induction equation (2.17e) yields in the ideal case ($\eta_0 = 0$)

$$\underline{a} \cdot \underline{B}_0 = 0. \tag{3.13}$$

Thus, an additional fraction of eigenmodes is again shifted to the origin. The problem of diagonalising the entire matrix by means of QR or QZ can be stabilised by introducing $a_\parallel = \underline{a} \cdot \underline{B}_0$ as a variable. Again the inverse iteration algorithm does solve the system accurately for all physical eigenvalues and eigenfunctions with $a_\parallel$ either kept or eliminated. Since dissipative systems are to be examined in the first place this point is not essential.

In conclusion, this discretisation produces a very accurate and numerically stable procedure as is demonstrated by the applications.

With the state vector for the perturbed quantities defined as

$$\underline{w}^T = (\rho, \underline{u}, T, \underline{a}) \tag{3.14}$$

the linear operators in Eqs. (2.17a)–(2.17c) and (2.17e) are represented by matrices **R** and **S**, where in **S** only the diagonal elements are nonzero and **R** contains differential operators and equilibrium quantities. The set of linearised equations then reads

$$\lambda \mathbf{S} w = \mathbf{R} w. \tag{3.15}$$

3. *Variables and Projections*

In the curvilinear flux coordinates s, χ, ϕ the ansatz is made for the perturbed velocity

$$\underline{u} = R^2 v_1 \nabla \chi \times \nabla \phi - \frac{iR^2}{f} v_2 \nabla \phi \times \nabla \psi - i \frac{R^2}{f} v_3 \underline{B}_0, \tag{3.16}$$

with f given by (3.2). Then v_3 represents basically the sound modes and v_1 and v_2 correspond to the contravariant velocity components. This leads to

$$\nabla \cdot (\underline{u}_\perp / R^2) \approx J^{-1} \left(\frac{\partial v_1}{\partial s} + m v_2 \right)_m \tag{3.17}$$

for every Fourier harmonic allowing us to make the fast wave contribution sufficiently small for unstable modes and for Alfvén modes. The divergence is brought to its required value by adjusting the component v_3. The perturbed vector potential is represented as

$$\underline{a} = -(i/f) a_1 \nabla \psi + a_2 \nabla \chi + a_3 \nabla \phi. \tag{3.18}$$

This leads to a simple form for the magnetic field

$$b^i = J^{-1} e^{ijk} \partial_j a_k. \tag{3.19}$$

Furthermore, we redefine the perturbed density and temperature

$$\begin{aligned} \bar{\rho} &= s\rho \\ \bar{T} &= sT. \end{aligned} \tag{3.20}$$

Then the state vector comprises the eight variables

$$\underline{w}^T = (\bar{\rho}, v_1, v_2, v_3, \bar{T}, a_1, a_2, a_3). \tag{3.21}$$

This leads to systems with total dimension

$$N = M \times 8 \times 2N_S = 16MN_S, \tag{3.22}$$

where M denotes the number of Fourier harmonics, N_S is the number of radial intervals and there are two orthogonal quadratic, resp. cubic, finite elements per interval.

4. *Eigenvalue Problem*

The system (2.17), summarised in matrix notation in Eq. (3.15) is solved in its weak form in the weighted residual formulation. Let

$$(\underline{z}, \underline{w}) = \int d\tau \underline{z}^* \cdot \underline{w} \tag{3.23}$$

denote an inner product in the appropriate Hilbert space. The exact solution is approximated by trial functions and mapped into the space of weighting functions; both function classes have to be sufficiently regular. We proceed by taking the inner product of the system (3.15) with the weighting function $\underline{z}$ by integrating over the volume

$$\lambda(\underline{z}, \mathbf{S}w) = (\underline{z}, \mathbf{R}\underline{w}). \tag{3.24}$$

Integration by parts reduces the order of derivatives. The error introduced in the differential equations through the approximation of $\underline{w}$ by a set of discrete expansion functions is orthogonal to every weighting function. In the standard Galerkin procedure adopted here the space of the weighting functions is chosen to coincide with that of the trial functions. This leads to the matrix eigenvalue problem

$$\mathbf{A}\underline{x} = \lambda\mathbf{B}\underline{x}, \tag{3.25}$$

where $\underline{x}$ denotes the vector of the expansion coefficients and the matrices $\mathbf{A}$ and $\mathbf{B}$ contain equilibrium quantities and derivatives and are bilinear in the trial functions. Obviously, the norm $\mathbf{B}$ is self-adjoint and positive definite, but $\mathbf{A}$ is always nonsymmetric even for $\eta_0 = 0$.

The Hermitian eigenproblem has all the properties needed to ensure successful numerical evaluation, since a Hermitian matrix cannot be defective and since a small perturbation in the matrix causes only a small perturbation in the eigenvalues. The general non-Hermitian system defines, therefore, a much harder problem, where small perturbations in the matrix can lead to a finite change of all eigenvalues (as discussed in the context of the pseudo spectrum [7]). Two different classes of solvers are applied to the system, namely QR (QZ), and inverse iteration. The diagonalisation by means of QR or QZ yields all eigenvalues but destroys the initial sparseness of $\mathbf{A}$ and $\mathbf{B}$. Therefore, at present it is used only up to a dimension of $N = 2000$. Nevertheless it yields valuable insight into the spectrum, especially when new branches with unknown properties are discovered. In conjunction with an out-of-core solver inverse iteration allows treatment of large systems, at present routinely up to $N = 50,000$ on a CRAY supercomputer and up to $N = 20,000$ on a typical workstation with 256 Mb memory and fast access to a disk. The features of these algorithms have been extensively discussed in Ref. [1].

IV. EVALUATION OF MATRIX ELEMENTS

We collect the contribution for the matrix elements for both norm and the "potential energy."

1. *Mass Conservation*

$$\lambda \iiint z(\hat{\rho})^* \cdot \hat{\rho} \frac{f}{s^2} \frac{R^2 q}{F} \, ds \, d\chi \, d\phi = -\iiint z(\hat{\rho})^* \cdot (\underline{u} \cdot \nabla \rho_0 + \rho_0 \nabla \cdot \underline{u}) J \, ds \, d\chi \, d\phi, \quad (4.1)$$

where $z(\hat{\rho})^*$ denotes the complex conjugate of the expansion of $\hat{\rho}$, i.e. $e^{-i\hat{m}\chi} h_{\hat{j}}(s)$. After the ϕ-integration we arrive at the integrands

$$K^{(1)} = z(\hat{\rho})^* \hat{\rho} \frac{f}{s^2} \frac{R^2 q}{F}, \quad (4.2)$$

$$\begin{aligned} W^{(1)} = -z(\hat{\rho})^* \frac{1}{s} \{ R^2 \rho_0 [\partial_s v_1 + (1/i)\partial_\chi (v_2 + v_3) + nq v_3] \\ + R^2 [v_1 \partial_s \rho_0 + (v_2 + v_3)(1/i)\partial_\chi \rho_0] \\ + \rho_0 [v_1 \partial_s R^2 + (v_2 + v_3)(1/i)\partial_\chi R^2] \}, \end{aligned} \quad (4.3)$$

where $\partial_s = \partial/\partial_s$, $\partial_\phi = \partial/\partial_\phi$, and $\partial_\chi = \partial/\partial_\chi$. Typically $\rho_0 = \rho_0(s)$ and the terms $\partial_\chi \rho_0$ vanish. The contributions to the **A** and **B** matrices still require the s, χ integration, e.g., $B^{(1)} = \iint ds \, d\chi \, K^{(1)}$. Making use of the general state vector $\underline{w}$ and inserting the finite-element basis vectors, i.e. cubic elements H for v_1, a_2, and a_3 and quadratic elements for $\hat{\rho}$, v_2, v_3, $\hat{T}$, and a_1, the contributions are labelled as

$$B(1, 1) = \iint ds \, d\chi \, e^{-i\hat{m}\chi} h_{\hat{j}}(s) \frac{f}{s^2} \frac{R^2 q}{F} e^{im\chi} h_j(s). \quad (4.4)$$

This expression describes the interaction of the weighting function $h_{\hat{j}}(s)e^{-im\chi}$ and the trial expansion function $h_j(s)e^{im\chi}$ and is symbolically abbreviated as

$$B(1, 1) = h \frac{f}{s^2} \frac{R^2 q}{F} h. \quad (4.5)$$

In this fashion the right-hand side of the mass conservation yields for the interaction of $z(\hat{\rho})^*$ and v_1,

$$A(1, 2) = -hH' \frac{R^2 \rho_0}{s} - hH \frac{1}{s} (R^2 \partial_s \rho_0 + \rho_0 \partial_s R^2), \quad (4.6)$$

where $H' = \partial_s H$. In the same fashion the expression $A(1, 3)$ and $A(1, 4)$, i.e. for the interaction of $z(\hat{\rho})^*$ with v_2 and v_3, are obtained.

It is noted that all matrix elements are bilinear expressions in the finite elements, where H, $H' = \partial_s H$, and h can be present on either side. The corresponding substructure is explained explicitly in Appendix C.

2. *Momentum Balance*

The momentum equation is cast into the form

$$\lambda \rho_0 \underline{u} = -\nabla \pi_1 + \underline{H}, \tag{4.7}$$

where π_1 denotes the total pressure

$$\pi_1 = \rho_0 T + \rho T_0 + \underline{B}_0 \cdot \underline{b} \tag{4.8}$$

with

$$\underline{B}_0 \cdot \underline{b} = \frac{|\nabla \psi|^2}{R^2} \left[\frac{1}{f}(na_1 - \partial_s a_3) - g(ma_3 - na_2) \right]$$
$$+ \frac{F}{R^2} \frac{1}{f} \frac{F}{q}(\partial_s a_2 - ma_1), \tag{4.9}$$

where

$$g = i \frac{\nabla \psi \cdot \nabla \chi}{|\nabla \psi|^2}. \tag{4.10}$$

For the evaluation of the matrix elements of the eigenvalue problem a vector is projected upon three orthogonal direction, i.e.

$$\underline{A} = \bar{A}_\psi \nabla \psi + \bar{A}_\perp \nabla \phi x \nabla \psi + \bar{A}_\phi \nabla \phi,$$

where the evaluation of the corresponding projections is straightforward.

The vector $\underline{H}$ has the corresponding components

$$\bar{H}_\psi = \bar{b}_\perp (\partial_\psi - ig\partial_\chi) \frac{|\nabla \psi|^2}{R^2} + F\bar{b}_\phi (\partial_\psi - ig\partial_\chi) \frac{1}{R^2}$$
$$- 2j_\phi \frac{\bar{b}_\perp}{R^2} + \frac{f}{J}(inq + \partial_\chi)\bar{b}_\psi, \tag{4.11a}$$

$$\bar{H}_\perp = \frac{f}{J}(\partial_\chi + inq)\bar{b}_\perp + j_\phi \bar{b}_\psi$$
$$+ \frac{F}{q|\nabla \psi|^2} \left[\bar{b}_\perp \partial_\chi \frac{|\nabla \psi|^2}{R^2} + F\bar{b}_\phi \partial_\chi \frac{1}{R^2} \right], \tag{4.11b}$$

$$\bar{H}_\phi = \frac{f}{J}(\partial_\chi + inq)\bar{b}_\phi + \frac{dF}{d\psi}|\nabla \psi|^2 \bar{b}_\psi. \tag{4.11c}$$

Here the three orthogonal projections of the magnetic field are defined as

$$\bar{b}_\psi = \frac{f}{j|\nabla \psi|^2}[\partial_\chi a_3 - ina_2] \tag{4.12a}$$

$$\bar{b}_\perp = \frac{1}{f}(na_1 - \partial_s a_3) + g(i\partial_\chi a_3 + na_2) \tag{4.12b}$$

$$\bar{b}_\phi = \frac{F}{fq}(\partial_s a_2 + i\partial_\chi a_1). \tag{4.12c}$$

The weak form of the momentum balance equation is given by

$$
\int W^{(2)} \, d\tau = \int d\tau \, \underline{z}(\underline{v})^* \cdot [\nabla \pi_1 + \underline{H}]
$$

$$
= \int d\tau \, \nabla \cdot \underline{v}^* \, \pi_1 - \int d\underline{S} \cdot \underline{z}(\underline{v})^* \, \pi_1 \tag{4.13}
$$

$$
+ \int d\tau \, \{ z(\underline{v}_\psi)^* \bar{H}_\psi |\nabla \psi|^2 + z(\bar{v}_\perp)^* \bar{H}_\perp |\nabla \psi|^2/R^2 + z(\bar{v}_\phi)^* \bar{H}_\phi /R^2 \}
$$

(where $z(v_1)^*$, $z(v_2)^*$, and $z(v_3)^*$ denote the complex conjugate of the expansion functions for v_1, v_2, and v_3) and is integrated by parts with

$$
\underline{z}(\underline{v})^* \cdot d\underline{S} = \underline{z}(\underline{v}_1)^* R^2 \, d\chi \, d\phi. \tag{4.14}
$$

It is noted that no second-order radial derivative on the expansion function occurs. Second-order χ-derivatives, which occur in the expression $\partial_\chi \bar{b}_\psi$, $\partial_\chi \bar{b}_\perp$, and $\partial_\chi \bar{b}_\phi$ are also integrated by parts.

3. *Energy Equation*

The energy equation is treated in the same manner as the continuity equation.

4. *Induction Equation*

The weak form leads to

$$
\int d\tau \, \underline{z}(\underline{a})^* \cdot (\underline{v} \times \underline{B}_0 - \eta_0 \nabla \times \nabla \times \underline{a})
$$

$$
= \int d\tau \, \underline{z}(\underline{a})^* \cdot \underline{v} \times \underline{B}_0 + \int \eta_0 \underline{z}(\underline{a})^* \times (\nabla \times \underline{a}) \cdot d\underline{S} \tag{4.15}
$$

$$
- \int d\tau \, \nabla \times \left(\eta_0 \underline{z}(\underline{a})^* \right) \cdot \nabla \times \underline{a}.
$$

Again second derivatives on the expansion functions are avoided by partial integration. The matrix elements in completeness are listed in Appendix A. The required equilibrium quantities are given in Appendix B.

5. *Implementation of the Boundary Conditions*

The boundary conditions at the magnetic axis imply

$$
v_1|_{\text{axis}} = 0; \quad a_2|_{\text{axis}} = 0; \quad a_3|_{\text{axis}} = 0. \tag{4.16}
$$

In the case of a perfectly conducting wall at the plasma boundary, it holds that

$$
v_1|_{\text{wall}} = 0; \quad a_2|_{\text{wall}} = 0; \quad a_3|_{\text{wall}} = 0. \tag{4.17}
$$

The boundary conditions (4.16) and (4.17) are essential boundary conditions. These must be applied to both the variables and test functions. In the CASTOR code the conditions are implemented by removing the rows and columns of the corresponding matrix elements on

the axis and at the boundary. Note that in this case the surface contributions in (4.13) and (4.15) are zero. We have developed a formulation where both the ideal and the resistive boundary conditions at the plasma–vacuum interface are implemented as natural boundary conditions; i.e., they are automatically satisfied when solving the weak form.

Using the pressure balance relation (2.23) and the absence of equilibrium surface currents (i.e., $\underline{B}_0 = \underline{B}_{0v}$) the surface contribution (4.13) becomes

$$W_s^I = -\int \underline{z}(\underline{v})^* \cdot d\underline{S}(\underline{B}_0 \cdot \underline{b}_v). \tag{4.18}$$

If we now perturb the vacuum with a unit field perturbation at the boundary, $\underline{b} \cdot \underline{n}_0 = \underline{b}_v \cdot \underline{n}_0$, the response of the vacuum in terms of the parallel magnetic perturbation, $\underline{B}_0 \cdot \underline{b}_v$, at the plasma boundary can be obtained. Thereby, the response of each independent Fourier harmonic perturbation ℓ is a function of the poloidal angle χ,

$$(\underline{B}_0 \cdot \underline{b}_v)_\ell = \sum_k \hat{\alpha}_{k\ell}(J\underline{b} \cdot \nabla s)_k, \tag{4.19}$$

where all the information of the vacuum solution is now described by the vacuum response matrix $\hat{\alpha}$. Rewritten in Fourier components (4.18) reads

$$W_s^I = -\int \left[z(v_1)^*\right]_{\hat{m}} e^{-i\hat{m}\chi} \sum_{k,\ell} \hat{\alpha}_{k\ell} e^{i\ell\chi} (Jb^1)_k R^2 \, d\chi. \tag{4.20}$$

The same procedure is followed for the resistive boundary condition, i.e. in the case of finite resistivity at the plasma boundary. Thereby the expression (4.18) for the ideal surface term is unchanged. This term in now used to implement the continuity of $\underline{B}_0 \cdot \underline{b}_v$. The resistive surface term (4.15) is utilised to implement the continuity of the remaining tangential component of the perturbed magnetic field,

$$W_s^R = -\int \eta_0(\underline{z}(a_2)^* b_{v3} - \underline{z}(a_3)^* b_{v2}) \, d\chi \, d\phi. \tag{4.21}$$

Again the vacuum response is defined by

$$\begin{aligned}
(b_{v3})_\ell &= \sum_k \hat{\beta}_{k\ell}(Jb^1)_k \\
(b_{v2})_\ell &= \sum_k \hat{\gamma}_{k\ell}(Jb^1)_k.
\end{aligned} \tag{4.22}$$

The matrices $\hat{\alpha}, \hat{\beta}$, and $\hat{\gamma}$ are related through

$$\underline{B}_0 \cdot \underline{b}_v = \frac{F}{qR^2}(b_{v2} + qb_{v3}). \tag{4.23}$$

The condition

$$J(\nabla \times \underline{b}) \cdot \nabla_S = 0 \quad \text{implies} \quad \frac{\partial b_{v3}}{\partial \chi} = \frac{\partial b_{v2}}{\partial \phi}. \tag{4.24}$$

So for the implementation of the boundary conditions only one of the three response matrices needs to be computed. The final form of the resistive surface term is

$$W_s^R = \int \eta_0 \cdot e^{-i\hat{m}\chi} \sum_{k,\ell} [\underline{z}(a_2)_{\hat{m}}^* \hat{\beta}_{k\ell} - \underline{z}(a_3)_{\hat{m}}^* \hat{\gamma}_{k\ell}] e^{i\ell\chi} (Jb^1)_k \, d\chi. \qquad (4.25)$$

In this fashion the resistive boundary conditions are implemented as natural boundary conditions and the ideal boundary conditions are retrieved by setting the resistivity to zero. The response matrix $\hat{\beta}$ is the only information required from the vacuum solution and can be calculated independently from the plasma normal-mode problem.

V. APPLICATIONS

A basic element in the development of the computer code is the testing of the numerical scheme, in particular, its accuracy and its convergence properties. Test cases in the cylindrical limit, which are available analytically and numerically as described in detail in Refs. [3, 8], were successfully reproduced but are not reported here. The first validation in toroidal geometry is based on the comparison with results from ideal MHD stability for a simple and easily reproducible tokamak equilibrium. These test cases were performed by different codes and published in Ref. [9] (1978), and were further utilised later on, e.g. by the NOVA code [10] (1987), and by the SPECTOR code [11] (1996).

In the CASTOR code the eigenvalue is normalised to the Alfvén time:

$$\hat{\lambda} = \lambda \frac{\sqrt{\rho(0)}R(0)}{B_0(0)}. \qquad (5.1)$$

The case of a constant pressure gradient $dp/d\psi$ and a constant current profile $F^{dF}/d\psi$ has an analytic solution as given by Solovev [12]. This class of tokamak equilibria allows for finite inverse aspect ratio $\varepsilon = a/R$, for elongation E, and for variable β_p (here β_p is set identically to unity). A JET-type cross section is given by $\varepsilon = 1/3$ and E = 2. The results computed by CASTOR are presented in Table 1, together with the previous results from the other codes. Here $\Lambda = R_W/a$ denotes the ratio of wall radius to plasma radius; $\Lambda = 1$ corresponds to a perfectly conducting wall placed at the plasma boundary; and $\Lambda = \infty$ corresponds to a wall at infinity. The values of the safety factor on axis $q(0)$ and on the boundary are also given. In this table the eigenvalues are normalised to the poloidal Alfvén time and thus the growth rates are multiplied by the value of the safety factor at the plasma surface, i.e.

$$\gamma = \hat{\lambda}q(1) = \lambda \frac{\sqrt{\rho(0)}R(0)q(1)}{B_0(0)}. \qquad (5.1b)$$

It is evident from this table that the results obtained from the different codes agree quite well. In the case of $\varepsilon^{-1} = 3$, E = 2, $\Lambda = 1$, and $q(0) = 0.7$ for example, the maximum deviation in the results in just 3 in 120 (2.5%). Similar agreement is obtained also in the other cases. We must remember that the first table in Ref. [9] was compiled in 1978 when the computing power was much less than today. In conclusion, the results computed by the CASTOR code agree within typically 1–3% with those from other codes as listed in Table 1.

TABLE 1
Comparison of the Eigenvalues γ^2 for Specific Solovev Equilibria
from Different Ideal MHD Spectral Codes

ε	E	Λ	q(0)	q(1)	n	CASTOR	KERNER	PEST-1	ERATO	Degtyarev	NOVA	Spector
1/6	1	2	1.791	2.0	1	0.216	0.202	0.204	—	0.211	0.208	—
1/6	1	2	2.239	2.5	1	0.513	0.504	0.506	—	0.511	0.508	—
1/3	2	1	0.3	0.522	2	0.429	0.413	0.427	0.431	0.430	0.430	0.432
1/3	2	1	0.7	1.219	2	0.12	0.118	0.119	0.120	0.121	0.119	0.118
1/3	2	∞	1.2	2.090	1	0.74	—	0.75	0.78	—	0.748	—
1/3	2	∞	2.0	3.483	1	0.66	—	0.68	0.75	—	0.656	—
1/3	2	∞	0.6	1.045	2	1.338	—	1.31	1.40	1.32	1.35	—
1/3	2	∞	1.0	1.741	2	1.03	—	1.03	1.07	1.06	1.038	—

This agreement is remarkable, since quite different numerical schemes were employed; e.g., ERATO utilises two-dimensional finite-elements in conjunction with a modification of the variational method (so-called finite hybrid element method), NOVA is based on a nonvariational formulation, together with a nonlinear root finder, whereas PEST and CASTOR use a Fourier finite-element discretisation, but CASTOR does not apply the variational form and SPECTOR uses finite differences.

In order to test the accuracy beyond the 1% margin obtained above, we perform a second comparison with the newly developed codes TERPSICHORE [13] and MARS [14], again for the Soloviev equilibrium by extending the Table 1 presented in Ref. [15]. For this second, more detailed comparison the eigenvalues in the normalisation on (5.1) are listed up to four digits in Table 2. Here two elliptical, E = 2, and one circular, E = 1, cross section have been considered for an inverse aspect ratio $\varepsilon = 1/3$, with fixed boundary $\Lambda = 1.0$. In the TERPSICHORE and MARS codes the accuracy of the piecewise finite-element method has been improved by the tuneable integration method [16]. The agreement with the CASTOR code is typically within 0.5% with the exception of one eigenvalue from the MARS code on the lower side ($\lambda = 0.0533$). In particular, the agreement between CASTOR and TERPSICHORE is within 1%.

Next the convergence properties are discussed. It is noted that from now on the normalisation as introduced in (5.1) is used. Since the eigenfunctions of the results from Table 1 are smooth a high order convergence with the number of radial finite elements, as well as with the number of Fourier harmonics, is expected. In Fig. 3 the eigenvalue is plotted versus the number of radial grid intervals N_s (labelled N on the figure) for different numbers of Fourier harmonics M. The dependence on the number of radial grid points is inversely quadratic and, hence, the convergence is fast. For this elliptical crosssection there is a strong coupling

TABLE 2
Comparison of the Eigenvalue λ for Specific Solovev Equilibria with $\varepsilon^{-1} = 3$
and $\Lambda = 1.0$ from Different Ideal MHD Spectral Codes

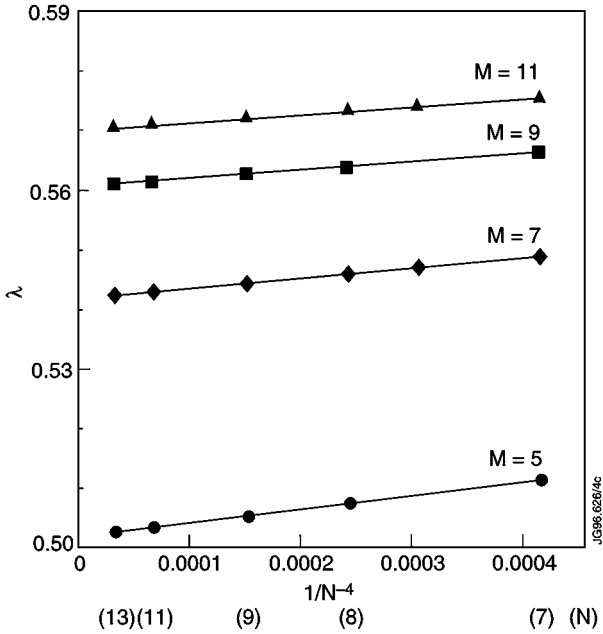| n	q(0)	E	CASTOR	ERATO	MARS	TERPSICHORE
2	0.3	2	1.255	1.26	1.26	1.25
2	0.7	2	0.284	0.284	0.284	0.284
3	0.75	1	0.05384	0.0541	0.0533	0.0538

FIG. 3. Convergence study with respect to the number of Fourier harmonics M and radial grid points N for the case $\varepsilon = 1/3$, $E = 2$, $\Lambda = \infty$, $q(0) = 1$, and $n = 2$ in Table 1. The dependence on the number grid points is inversely quartic.

due to ellipticity with $\Delta m = 2$ and a weak toroidal coupling with $\Delta m = 1$. The overall convergence with respect to the number of Fourier harmonics is therefore slow and requires more than 20 harmonics for a good approximation to the final result. But the convergence is asymptotically faster than a polynomial dependence in $1/M$. The expected exponential behaviour is displayed in Fig. 4 for the case of $\varepsilon = 1/3$ and $E = 1$ in the Solovev equilibrium. The error scales as $e^{-M/1.75}$.
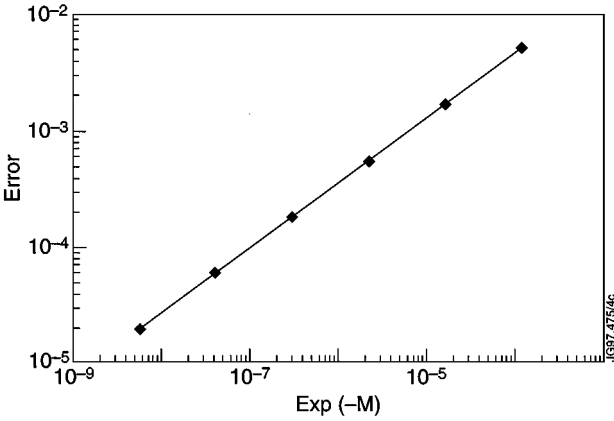

FIG. 4. Convergence study with respect to the number of Fourier harmonics M for fixed N (N = 15) for the case of $\varepsilon = 1/3$, $E = 1$, $q(0) = 0.75$, $n = 3$, and $\Lambda = 1.0$. The convergence exhibits exponential dependence in M.
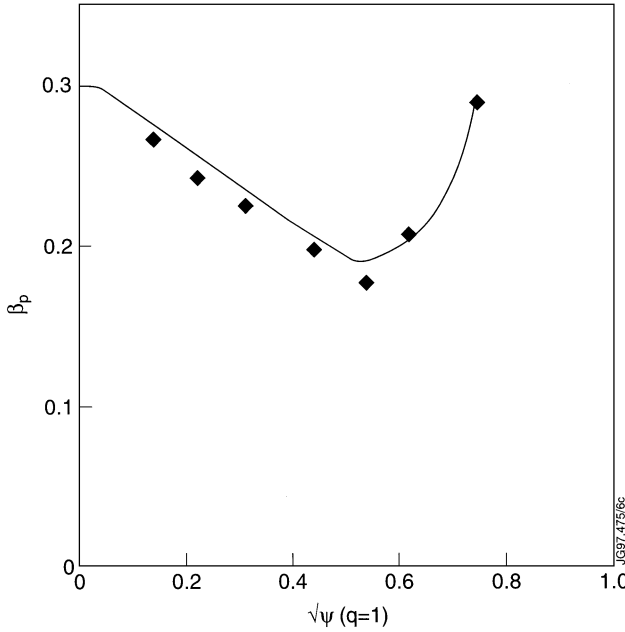
FIG. 5. Stability limit for the internal kink mode in terms of $\beta_p = 2(\int pdA/\int dS - p(\psi_1))/B_p^2(\psi_1))$ versus the radius of the $q = 1$ surface for a circular cross section large aspect ratio, $\varepsilon^{-1} = 10$, equilibrium with profiles given by (5.2a), (5.2b) in comparison with the limits from analytic theory of Ref. [19].

A severe test for the validation of a MHD stability code is given by the interval kink mode, which has different stability properties for cylindrical and toroidal symmetry. Consequently, the stability is determined by fine details of the tokamak configuration where terms up to second order in inverse aspect ratio need to be retained and analytical treatment needs to be carried through order ε^4 in δW. A toroidal equilibrium with circular cross section and aspect ratio $\varepsilon^{-1} = 10$ is analysed. The choice of the pressure and current profile

$$p = p_0(1 - \bar{\psi}), \tag{5.2a}$$

$$\langle j \rangle = j_0(1 - \bar{\psi}), \tag{5.2b}$$

allows a comparison with analytical work by Bussac *et al.* [17] and Mikhailovskii [18].

In Fig. 5 the stability limit in terms of β_p, defined according of Refs. [17, 18] as

$$\beta_p = 2\frac{\int pdA/\int dS - p(\psi_1)}{B_p^2(\psi_1)}, \tag{5.3}$$

where $dA = J \, ds \, d\chi$ and $B_p(\psi_1)$ is the flux-averaged poloidal field, is displayed as a function of the radius of the $q = 1$ surface. The limit for $q(0) = 1.0$ is given by $\beta_p = 0.3$. For a small radius of the $q = 1$ surface, i.e. $s(q = 1) < 0.25$, our results coincide with the analytical results derived for the parabolic current profile $j(r) = j_0(1 - r^2/a^2)$. The detailed comparison requires the integration of the second-order ODE given in Ref. [19] for the profile (5.2b), where the detailed equilibrium relation $\psi = \psi(r)$ is utilised to relate with the corresponding $j(r)$ in the analytic model. These analytic marginal points are shown as the solid line in Fig. 5.

The minimum β_p value is defined by the configuration where q(1) = 2.0 i.e. yielding a critical β_p slightly below the value 0.2. When the q = 2 surface is no longer inside the plasma the predicted stabilising effect becomes dominant as is evident from the part of the diagram with s (q = 1) > 0.55. Each point on Fig. 5 is obtained by extrapolating β_p to its value where λ is zero as demonstrated in Fig. 6. It is emphasised that growth rates in the order of Re $\lambda \approx 10^{-4}$ to 10^{-5} are still evaluated with good accuracy. Three Fourier components m = 0, 1, and 2 need to be included. The numerical calculations are thus performed with five harmonics ranging from −1 to 3. Near marginal stability, where the eigenvalue approaches the Alfvén continuum, the eigenfunction develops a singular behaviour in radius. Therefore, a high resolution with respect to the number of radial grid points is necessary. The case of N = 1000 constitutes the accurate solution λ_∞. In Fig. 7 the deviation of λ from this asymptotic solution is plotted versus $1/N_s$ in the double logarithmic scale. The maximum deviation defines a straight line which scales approximately as $1/N_S^4$.

Next we consider nonzero resistivity. In the case that the ideal internal kink mode is stable there exist unstable resistive internal kink modes. This is shown in Fig. 8. In a slightly different tokamak equilibrium with circular cross section, aspect ratio $\varepsilon^{-1} = 10$, and the profiles

$$p = p_0(1 - \bar{\psi}),$$
$$\langle j \rangle = j_0(1 - \bar{\psi}),$$

(5.4)

with $q_0 = 0.9$ and $\beta_p = 0.1$, the growth rate is plotted in dependence of the resistivity. The two branches of the resistive n = 1 perturbation are displayed, namely the tearing mode scaling as $\eta_0^{3/5}$ and the resistive interchange scaling as $\eta_0^{1/3}$. For very small values of the
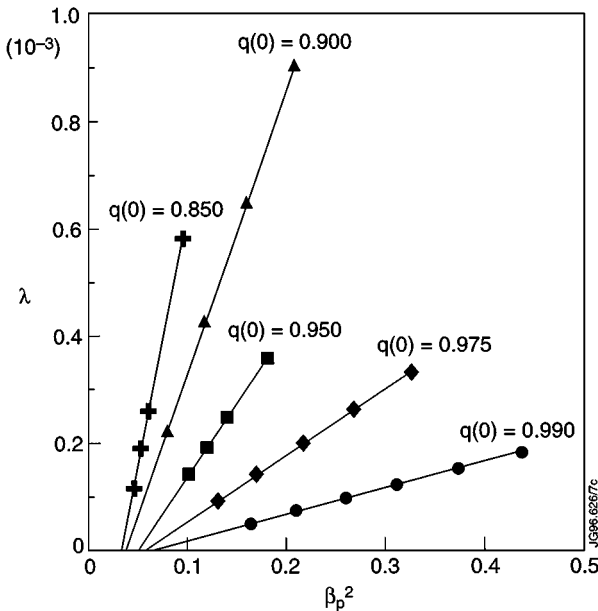

FIG. 6. The extrapolation to marginal stability of the internal kink mode for different values of q(0) displayed in Fig. 5.
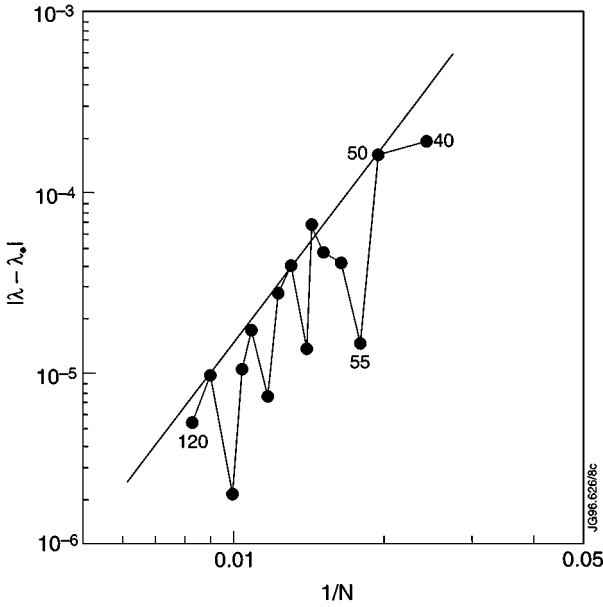
FIG. 7. Deviation of the growth rate from the converged growth rate λ_∞ (defined by N = 1000) obtained with five harmonics $-1 \leq M \leq 3$ for q(0) = 0.9 and $\beta_p = 0.4$ in a double logarithmic scale. The maximum deviation defines a straight line scaling as $1/N^4$.

resistivity the pressure driven instability becomes dominant (in this case for $\eta_0 \lesssim 10^{-12}$). It is emphasised that η_0 values as small as 10^{-14} need to be treated in order to obtain the correct asymptotic scaling. The necessary accuracy in the numerical calculation is achieved by including up to $N_s = 1000$ radial points in conjunction with mesh accumulation around
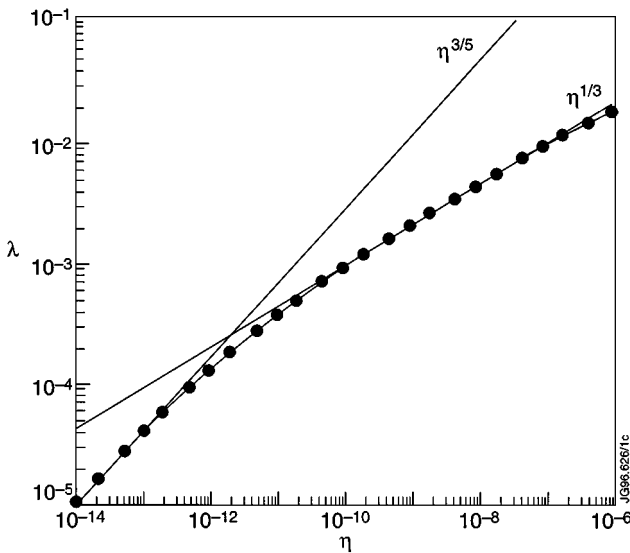

FIG. 8. Growth rate of the resistive internal kink for the equilibrium with circular cross section, $\varepsilon^{-1} = 10$ and the profiles given in (5.4); q(0) = 0.9 and $\beta_p = 0.1$. Two branches scaling as $\eta_0^{3/5}$ and $\eta_0^{1/5}$, respectively, exist in the limit of small resistivity.

the q $= 1$ and 2 surfaces. The growth rates being as low as 10^{-5} have been obtained by convergence studies as discussed above. A detailed study of resistive instabilities in a tokamak is given in Refs. [20, 21].

In the final application the stable part of the resistive Alfvén spectrum is examined. Again a tokamak with circular cross section is considered. The toroidal coupling introduces gaps in the ideal Alfvén continua and global modes exist with a frequency inside the gap (see Ref. [22]). The aspect ratio and magnetic shear are chosen such that there is a single, pronounced gap; this is achieved by a tight aspect ratio, $\varepsilon = 0.3$, and small shear with the safety factor ranging from $q_0 = 1.25$ on the axis to $q_s = 1.75$ on the boundary. For a toroidal wave number n $= 1$ there is a gap in the m $= 1$ and 2 spectrum around the $q_{gap} = 1.5$ surface which occurs near the half radius s ≈ 0.5. In Fig. 9a the complex Alfvén spectrum is displayed for two Fourier harmonics m $= 1$ and 2 and a resistivity of $\eta_0 = 10^{-5}$. The Alfvén modes are now heavily damped, yielding two curves in the complex λ-plane. These curves are actually independent of the value of resistivity. But the point density scales as $\eta_0^{-1/2}$. The resistive branch joins the ideal continua only at the end points of the two continua, as is known from many analytical and numerical studies (see Refs. [3, 7, 8]). The gap in the two ideal continua ranging from $0.29 \leq \text{Im}(\lambda) \leq 0.46$ is clearly visible. There is a global TAE with a frequency of $\text{Im}(\lambda) = 0.34$. The entire resistive Alfvén spectrum is well resolved. It is noted that the slow modes have much smaller frequency and lie in this scale basically on the real λ-axis. In Fig. 9b the frequency, i.e. $\omega = \text{Im}\{\lambda\}$, is plotted as a function of the radial coordinate s. The ideal continua are indiated by the thick lines. For finite resistivity the continuum is replaced by the discrete set shown in Fig. 9a. For small $\omega \sim 0.2$ the eigenfunction has basically only one Fourier component, namely a m $= 1$ for small s and a m $= 2$ for large s. Accordingly, for $\omega \sim 0.6$ the m $= 2$ component is dominant at small s and the m $= 1$ at large s. Near the lower and upper end of the gap both harmonics have equal weight. The eigenfunctions of three normal modes are displayed as a function of the radius at their corresponding frequency value. The solution with a frequency inside the gap, case 2 in Fig. 9, is the TAE and has even parity in the m $= 1, 2$ components. The mode with a frequency at the top of the gap, case 1 in Fig. 9, corresponds to the first kinetic toroidal Alfvén eigenmode (KTAE) and has odd parity. Both types of Alfvén eigenmodes play a pronounced role in the discussion of Alfvén eigenmode induced anomalous α-particle transport in deuterium–tritium plasmas (see Ref. [23]).

VI. CONCLUSION

The resistive MHD normal-mode spectrum in tokamaks, i.e. the linear motion around a general axisymmetric equilibrium, is solved numerically by the CASTOR code. The numerical scheme is based on a specific flux-coordinate system and on an appropriate choice for the projection of the perturbed velocity and the magnetic field in the form of the vector potential. A Fourier finite-element discretisation is applied to the perturbation leading to a large-scale non-Hermitian eigenvalue problem. It is shown that both the ideal MHD as well as the resistive MHD spectrum is approximated with high accuracy. The challenge for the numerical method consists of resolving the limit of asymptotically small resistivity well.

The benchmark tests yield good agreement (typically within 1%) with other MHD codes. The studies of the internal kink instability (both the ideal and resistive mode) demonstrate
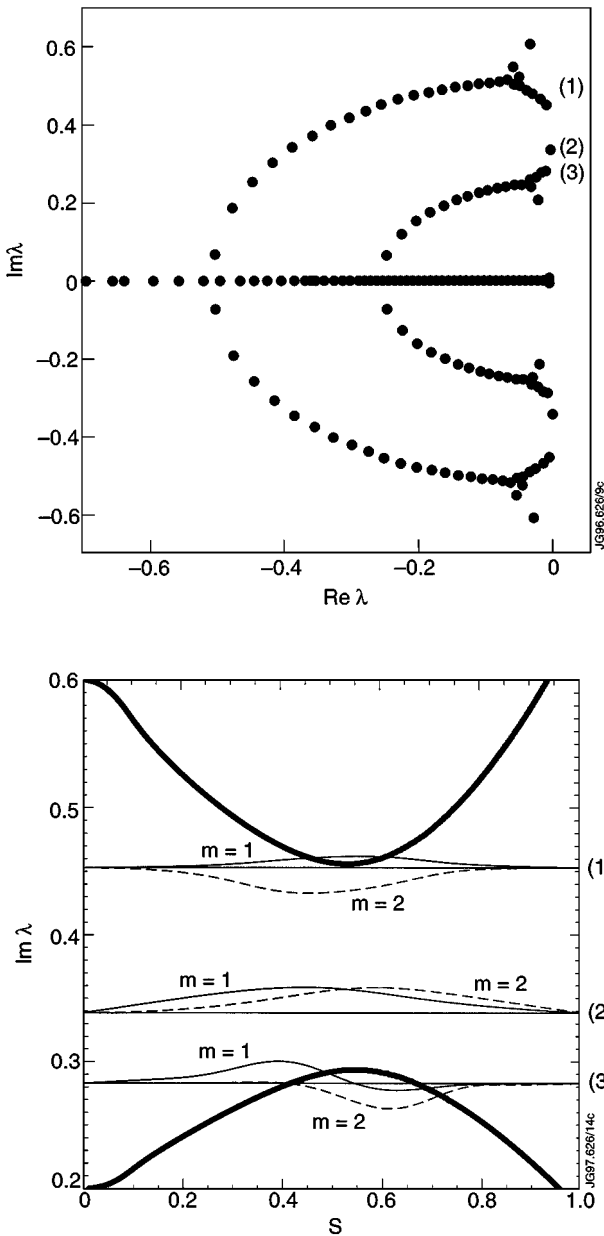
FIG. 9. (a) The complex resistive spectrum of a configuration with a tight aspect ratio case, $\varepsilon = 0.3$, circular cross section, and a weak shear profile ($q_0 = 1.25$, $q_s = 1.75$) for $\eta_0 = 10^{-5}$. For the toroidal wave number $n = 1$ a single pronounced gap in the Alfvén spectrum occurs at $q_G = 1.5$ with a TAE inside this gap. (b) The ideal Alfvén frequencies ($m = 1$, 2 continua) $\omega = \text{Im}(\lambda)$ are presented as a function of radius (thick lines). Three eigenfunctions of the resistive spectrum are displayed at the position of their frequency.

that the code evaluates small growth rates with high accuracy and for finite resistivity the correct scaling for asymptotically small resistivity.

In Fourier space the convergence of the eigenvalue is asymptotically faster than a polynomial dependence in $1/M$. The convergence with respect to the number of radial finite elements yields typically an inversely quartic dependence; i.e., $|\lambda_\infty - \lambda_N| \propto 1/N_s^4$.

The CASTOR code is used routinely for modelling JET discharges. The emphasis has been on the beta limits, kink-type instabilities, and on stable Alfvén eigenmodes. The numerical method provides a general tool for the evaluation of the spectrum of dissipative MHD systems. Consequently, a generalisation of the method to the analysis of kinetic Alfvén eigenmodes [23] and of thermal instabilities has been successfully performed in the context of a stability analysis of tokamak equilibria concerning MARFE's [24].

APPENDIX A: MATRIX ELEMENTS

The matrix elements are bilinear expressions in the expansion functions and are labelled $B(i, j)$ and $A(i, j)$, respectively, with $i, j = 1, \ldots, 8$. The Fourier exponents are $e^{-i\hat{m}\chi}$ and $e^{im\chi}$ for $\hat{m}, m \in [M_{min}, M_{max}]$. The radial expansion function is $h_k^i(s), i = 1, \ldots, 8$ and $k = 1, \ldots, N_s$, and either quadratic (labelled h) or cubic elements (labelled H) are employed. The equilibrium quantities are in general χ-dependent and are Fourier-spline interpolated:

$$eq(s, \chi) = \sum_\ell e^{i\ell\chi} \overline{eq}_\ell(s) \tag{A.1}$$

Thus a typical matrix element reads

$$B(i, j) = \int d\phi \, d\chi \, ds \, e^{-i\hat{m}\chi} h_k^i(s) \, eq(s, \chi) h_k^j(s) e^{im\chi}. \tag{A.2}$$

The ϕ and χ integrations are then performed analytically and the remaining s integration is done numerically by 4-point Gaussian quadratures. In the following only the integrand is listed, e.g.

$$B(i, j) \rightarrow h^i eq(s, \chi) h^j,$$

where

$$h^i, h^j \in \{h, H',\} \quad \text{with } H' = \partial H / \partial S.$$

The correspond substructure due to the radial overlap of the neighbouring finite elements is explained in Appendix C.

The matrix elements are

$$B(1, 1) = hh \frac{fqR^2}{s^2 F}$$

$$B(2, 2) = HH\rho_0 \left(\frac{fFR^2}{q} \frac{1}{|\nabla\psi|^2} + \frac{fqR^4}{F} \frac{(\nabla\psi \cdot \nabla\chi)^2}{|\nabla\psi|^2} \right)$$

$$B(2, 3) = Hh\rho_0 i \frac{qR^4}{F} (\nabla\psi \cdot \nabla\chi)$$

$$B(2, 4) = B(2, 3)$$

$$B(3, 2) = -B(2, 3)$$

$$B(3, 3) = hh\rho_0 \frac{qR^4}{fF} |\nabla\psi|^2$$

$$B(3, 4) = B(3, 3)$$

$$B(4, 2) = -B(2, 3)$$

$$B(4, 3) = B(3, 3)$$

$$B(4, 4) = hh\rho_0 \left(\frac{qR^4}{fF} |\nabla\psi|^2 + \frac{FqR^4}{f} \right)$$

$$B(5, 5) = hh\frac{1}{\gamma - 1}\rho_0 \cdot \frac{fqR^2}{s^2F}$$

$$B(6, 6) = hh\frac{qR^2}{fF}|\nabla\psi|^2$$

$$B(6, 7) = hHi \cdot \frac{qR^2}{F}(\nabla\psi \cdot \nabla\chi)$$

$$B(7, 6) = -B(6, 7)$$

$$B(7, 7) = HH\left(\frac{fF}{q} \cdot \frac{1}{|\nabla\psi|^2} + \frac{fqR^2}{F}\frac{(\nabla\psi \cdot \nabla\chi)^2}{|\nabla\psi|^2} \right)$$

$$B(8, 8) = HH\frac{fq}{F}$$

$$A(1, 2) = -hH'\frac{\rho_0 R^2}{s} - hH\frac{1}{s}\left(R^2\frac{\partial \rho_0}{\partial s} + \rho_0\frac{\partial R^2}{\partial s} \right)$$

$$A(1, 3) = -hh\frac{\rho_0}{s}\hat{m}R^2$$

$$A(1, 4) = -hh\frac{\rho_0 R^2}{s}(\hat{m} + nq)$$

$$A(2, 1) = Hh\frac{T_0}{s}\frac{\partial R^2}{\partial s} + H'h\frac{T_0 R^2}{s}$$

$$A(2, 5) = Hh\frac{\rho_0}{s}\frac{\partial R^2}{\partial s} + H'h\frac{\rho_0 R^2}{s}$$

$$A(2, 6) = H'h\left(\frac{n}{f}|\nabla\psi|^2 - \frac{F^2}{fq} \cdot m \right) - H'h\left[n \cdot i(2\hat{m} - m + nq) \cdot (\nabla\psi \cdot \nabla\chi) \right.$$

$$\left. + \frac{F^2 n}{q^2 f}\frac{\partial}{\partial s}\left(\frac{q^2}{F^2}|\nabla\psi|^2 \right) \right]$$

$$A(2, 7) = H'H'\frac{F^2}{fq} + H'H\,in(\nabla\psi \cdot \nabla\chi)$$

$$+ HH\left[\frac{nF^2}{q^2}(\hat{m} + nq)\left(\frac{f}{R^2|\nabla\psi|^2} + \frac{fq^2}{F^2}\left(\frac{\nabla\psi \cdot \nabla\chi}{\nabla\psi} \right)^2 \right) \right.$$

$$\left. + in \cdot (\nabla\psi \cdot \nabla\chi) \cdot \frac{q}{F} \cdot \frac{\partial}{\partial s}\left(\frac{F}{q} \right) \right]$$

$$A(2, 8) = -H'H'\frac{1}{f}|\nabla\psi|^2 - H'H\,\mathrm{im}(\nabla\psi\cdot\nabla\chi)$$

$$+ HH'\left[i(2\hat{m} - m + nq)(\nabla\psi\cdot\nabla\chi) + \frac{F^2}{fq^2}\frac{\partial}{\partial s}\left(\frac{q^2}{F^2}|\nabla\psi|^2\right)\right]$$

$$- HH\left[m\frac{F^2}{q^2}(\hat{m} + nq)\left(\frac{f}{R^2|\nabla\psi|^2} + \frac{fq^2}{F^2}\left(\frac{\nabla\psi\cdot\nabla\chi}{\nabla\psi}\right)^2\right)\right.$$

$$\left. + \hat{m}i(\nabla\psi\cdot\nabla\chi)\frac{q}{F}\cdot\frac{\partial}{\partial s}\left(\frac{F}{q}\right)\right]$$

$$A(3, 1) = hh\frac{mT_0R^2}{s}$$

$$A(3, 5) = hh\frac{m\rho_0R^2}{s}$$

$$A(3, 6) = -hh\left(m\hat{m}\frac{F^2}{fq} + n^2\frac{q}{f}\cdot|\nabla\psi|^2\right)$$

$$A(3, 7) = hH'\frac{\hat{m}F^2}{fq} + hH\left[-in(m - \hat{m} + nq)\nabla\psi\cdot\nabla\chi + n\frac{F}{fq}\frac{\partial}{\partial s}\left(\frac{q}{F}|\nabla\psi|^2\right)\right]$$

$$A(3, 8) = hH'n\cdot\frac{q}{F}|\nabla\psi|^2 + hH\left[im(m - \hat{m} + nq)\nabla\psi\cdot\nabla\chi - \frac{F}{fq}\cdot\frac{\partial}{\partial s}\left(\frac{q}{F}|\nabla\psi|^2\right)\right]$$

$$A(4, 7) = hH'\frac{F^2}{fq}(\hat{m} - m) + hHn\left[(\hat{m} - m)i\nabla\psi\cdot\nabla\chi + \frac{F}{fq}\frac{\partial}{\partial s}\left(\frac{q}{F}|\nabla\psi|^2\right) + \frac{F}{f}\cdot\frac{dF}{ds}\right]$$

$$A(4, 8) = -hHm\left[i(\hat{m} - m)\nabla\psi\cdot\nabla\chi + \frac{F}{fq}\cdot\frac{\partial}{\partial s}\left(\frac{q}{F}|\nabla\psi|^2\right) + \frac{F}{f}\cdot\frac{dF}{ds}\right]$$

$$A(5, 2) = -hH'\frac{R^2\rho_0T_0}{s} - hH\frac{\rho_0}{s}\left(T_0\frac{\partial R^2}{\partial s} + \frac{R^2}{\gamma - 1}\frac{\partial T_0}{\partial s}\right)$$

$$A(5, 3) = -hh\frac{R^2\rho_0T_0}{s}\hat{m}$$

$$A(5, 4) = -hh\frac{R^2\rho_0T_0}{s}(\hat{m} + nq)$$

$$A(6, 2) = -hH\cdot iq(\nabla\psi\cdot\nabla\chi)$$

$$A(6, 3) = hh\frac{q}{f}R^2\cdot|\nabla\psi|^2$$

$$A(6, 6) = hh\left(-n^2\eta_0\frac{q}{fF}|\nabla\psi|^2 - m^2\cdot\frac{F}{fq}\right)$$

$$A(6, 7) = hH'\eta_0m\cdot\frac{F}{fF} - hH\,in^2\nabla\psi\cdot\nabla\chi\,\eta_0\frac{q}{F}$$

$$A(6,8) = hH'\eta_0 n \frac{q}{fF}|\nabla\psi|^2 + hH \cdot i \cdot nm\eta_0 \frac{q}{F}\nabla\psi \cdot \nabla\chi$$

$$A(7,2) = -HH\frac{F^2}{q}\left(\frac{f}{|\nabla\psi|^2} + \frac{fq^2R^2}{F^2}\frac{(\nabla\psi \cdot \nabla\chi)^2}{|\nabla\psi|^2}\right)$$

$$A(7,3) = -Hhiq(\nabla\psi \cdot \nabla\chi)$$

$$A(7,6) = H'h\eta_0\frac{F}{fq}m + Hh\left[in^2\eta_0\frac{q}{F}\nabla\psi \cdot \nabla\chi + \frac{F}{fq}m\frac{\partial\eta_0}{\partial s}\right]$$

$$A(7,7) = -H'H'\eta_0\frac{F}{fq} - HHn^2\eta_0 \cdot \frac{fF}{q}\left(\frac{1}{R^2|\nabla\psi|^2} + \frac{q^2}{F^2}\frac{(\nabla\psi \cdot \nabla\chi)^2}{|\nabla\psi|^2}\right) - HH'\frac{F}{fq}\frac{\partial\eta_0}{\partial s}$$

$$A(7,8) = -HH'in\eta_0\frac{q}{f}(\nabla\psi \cdot \nabla\chi) + HH\frac{\eta_0Ff}{q}mn\left(\frac{1}{R^2|\nabla\psi|^2} + \frac{q^2}{F^2}\frac{(\nabla\psi \cdot \nabla\chi)^2}{\nabla\psi^2}\right)$$

$$A(8,6) = H'hn\eta_0 \cdot \frac{q}{fF} \cdot |\nabla\psi|^2 - Hh\left[i\frac{q}{F}\eta_0 n\hat{m}\nabla\psi \cdot \nabla\chi + n \cdot \frac{q}{fF} \cdot |\nabla\psi|^2 \cdot \frac{\partial\eta_0}{\partial s}\right]$$

$$A(8,7) = H'Hin\frac{\eta_0q}{F}\nabla\psi \cdot \nabla\chi + HH\left[\eta_0 n\hat{m} \cdot \frac{fF}{q}\left(\frac{1}{R^2|\nabla\psi|^2} + \frac{q^2}{F^2}\frac{(\nabla\psi \cdot \nabla\chi)^2}{|\nabla\psi|^2}\right)\right.$$

$$\left. + in\frac{q}{F} \cdot (\nabla\psi \cdot \nabla\chi) \cdot \frac{\partial\eta_0}{\partial s}\right]$$

$$A(8,8) = -H'H'\eta_0\frac{q}{fF} \cdot |\nabla\psi|^2 + HH'\left[\frac{q}{F}\eta_0\hat{m}(\nabla\psi \cdot \nabla\chi) - \frac{q}{fF}|\nabla\psi|^2\frac{\partial\eta_0}{\partial s}\right]$$

$$- H'Hi\eta_0 m \cdot \frac{q}{F} \cdot (\nabla\psi \cdot \nabla\chi)$$

$$- HH\left[\eta_0 m\hat{m} \cdot \frac{fF}{q}\left(\frac{1}{R^2|\nabla\psi|^2} + \frac{q^2}{F^2}\frac{(\nabla\psi \cdot \nabla\chi)^2}{|\nabla\psi|^2}\right)\right.$$

$$\left. - im\frac{q}{F}(\nabla\psi \cdot \nabla\chi)\frac{\partial\eta_0}{\partial s}\right].$$

The ideal boundary conditions yield the contribution at $s = 1$ to the matrix elements

$$A(2,7) = \frac{iF}{q}(\hat{m} + nq)\hat{\beta}_{\hat{m}m}$$

$$A(2,8) = \frac{-im}{n}\frac{F}{q}(\hat{m} + nq)\hat{\beta}_{\hat{m}m} \quad (\text{for } n \neq 0).$$

For finite resistivity the corresponding contributions are

$$A(7,7) = -i\eta_0 n\hat{\beta}_{\hat{m}m}$$

$$A(7,8) = \eta_0 m\beta_{\hat{m}m}$$

$$A(8, 7) = \eta_0 \hat{m} \beta_{\hat{m}m}$$

$$A(8, 8) = -i\eta_0 \frac{m\hat{m}}{n} \hat{\beta}_{\hat{m}m} \text{ (for } n \neq 0).$$

APPENDIX B: EQUILIBRIUM QUANTITIES

In the curvilinear flux coordinate system the line element is given by $d\underline{s} = ds\underline{e}_1 + d\chi\underline{e}_2 + d\phi\underline{e}_3$, where $\underline{e}_1 = J\nabla\chi \times \nabla\phi$ etc. The distance along a magnetic field line with $ds = 0$ is represented by its projections

$$d\ell_\phi = \sqrt{g_{33}} \, d\phi \text{ (for } d\chi = 0) \text{ with } g_{33} = R^2$$
$$d\ell_p = \sqrt{g_{22}} \, d\chi \text{ (for } d\phi = 0). \tag{B.1}$$

The ratio is determined by the magnetic components

$$\frac{d\ell_\phi}{d\ell_p} = \frac{Rd\phi}{d\ell_p} = \frac{B_\phi}{B_p}, \tag{B.2}$$

which implies

$$d\chi = \frac{F(s)}{q(s)} \frac{d\ell_p}{R|\nabla\psi|}. \tag{B.3a}$$

Thus, integrating along a flux contour $s = ct$ and evaluating $d\ell_p$ in a local coordinate system χ is determined,

$$\chi = \frac{F(s)}{q(s)_s} \int \frac{d\ell_p}{R|\nabla\psi|}. \tag{B.3b}$$

The equilibrium code HELENA solves the Grad–Shafranov equation for the poloidal flux ψ,

$$\Delta^*\psi = \frac{\partial^2\psi}{\partial x^2} + \frac{\partial^2\psi}{\partial y^2} - \frac{1}{1+\varepsilon x}\frac{\partial\psi}{\partial x} = -(1+\varepsilon x)^2\frac{dP(\psi)}{d(\psi)} - \frac{1}{2}\frac{dF^2(\psi)}{d(\psi)}, \tag{B.4}$$

where $x = (R - R_0)/a$, $y = Z/a$ are the normalised coordinates in the poloidal plane and $\varepsilon (= a/R_0)$ is the inverse aspect ratio. Equation (B.4) has to be solved inside a region with an arbitrary but given plasma boundary, where the boundary condition states that $\psi = \psi_B$.

The Grad–Shafranov equation is solved by applying the Galerkin procedure using bicubic isoparametric finite elements, which yields highly accurate solutions with both ψ and $\nabla\psi$ continuous across element boundaries. This leads to a system of linear equations for each step of the nonlinear iteration:

$$K\psi_{n+1} = b_n. \tag{B.5}$$

K denotes the stiffness matrix and $\underline{b}$ is the force vector given by

$$K_{ij} = \iint \frac{1}{R}\nabla H_i(\xi, t) \cdot \nabla H_j(\xi, t) J \, d\zeta \, dt,$$
$$b_i = \iint H_i(\xi, t)\left[Rp'(\psi) + \frac{1}{2}\frac{1}{R}(F^2(\psi))'\right] J \, d\zeta \, dt, \tag{B.6}$$

where J is the Jacobian $\partial(x, y)/\partial(\xi, t)$ and H_i are the interpolating functions. The integration is done numerically using a 4 by 4 point Gaussian quadrature. Details of the iteration of Eq. (B.5) are given by [25].

The interpolating functions of the bicubic Hermite element are given by

$$H_{00}(x, y) = \frac{1}{16}(x + x_0)^2(xx_0 - 2)(y + y_0)^2(yy_0 - 2)$$

$$H_{10}(x, y) = -\frac{1}{16}x_0(x + x_0)^2(xx_0 - 1)(y + y_0)^2(yy_0 - 2)$$

$$H_{01}(x, y) = -\frac{1}{16}(x + x_0)^2(xx_0 - 2)y_0(y + y_0)^2(yy_0 - 1)$$

$$H_{11}(x, y) = \frac{1}{16}x_0(x + x_0)^2(xx_0 - 1)y_0(y + y_0)^2(yy_0 - 1),$$

(B.7)

with x_0 and y_0 the coordinates of the four corners of a unit element $(-1, -1)$, $(-1, 1)$, $(1, 1)$, and $(1, -1)$. A function $f(x, y)$ inside the element is then approximated by

$$f(x, y) = \sum_{x_0, y_0} H_{00}(x, y)f(x_0, y_0) + H_{10}(x, y)\frac{\partial f}{\partial x}(x_0, y_0)$$
$$+ H_{01}(x, y)\frac{\partial f}{\partial y}(x_0, y_0) + H_{11}(x, y)\frac{\partial^2 f}{\partial y\,\partial x}(x_0, y_0),$$

(B.8)

where the summation is over the four corners of the element. However, with the elements directly defined in (x, y) coordinates it is impossible to approximate the shape of the plasma boundary accurately or even continuously.

Isoparametric mapping provides a one-to-one correspondence between the local (ζ, t) and the global (x, y) coordinates. The coordinates transformation between the bi-unit square and the curvilinear element is given by

$$x(\zeta, t) = \sum_{\zeta_0, t_0} \left[H_{00}x_{\zeta_0, t_0} + H_{10}\frac{\partial x_{\zeta_0, t_0}}{\partial \zeta} + H_{10}\frac{\partial x_{\zeta_0, t_0}}{\partial t} + H_{11}\frac{\partial^2 x_{\zeta_0, t_0}}{\partial \zeta\,\partial t} \right]$$

$$y(\zeta, t) = \sum_{\zeta_0, t_0} \left[H_{00}y_{\zeta_0, t_0} + H_{10}\frac{\partial y_{\zeta_0, t_0}}{\partial \zeta} + H_{10}\frac{\partial y_{\zeta_0, t_0}}{\partial t} + H_{11}\frac{\partial^2 y_{\zeta_0, t_0}}{\partial \zeta\,\partial t} \right],$$

(B.9)

where ζ_0, t_0 are the coordinates of the four corners of a unit element. The same interpolation function H_{ij} $(i, j = 0, 1)$ are used to approximate the flux within the elements. The given radius of the plasma boundary is represented by a Fourier series

$$a_B(\theta) = \sum_m a_m e^{im\theta},$$

where θ is, e.g., the polar angle. A global coordinate system is constructed by

$$x = \tilde{f}(r)a_B(\theta)\cos(\theta)$$
$$y = \tilde{f}(r)a_B(\theta)\sin(\theta),$$

(B.10)

where the radial coordinate $\tilde{f}$ is an arbitrary function ranging from 0 in the centre to 1 on the boundary. By identifying the local ζ coordinate with the global $\tilde{f}(r)$ coordinate, i.e. $\zeta = \zeta(\tilde{f})$ and t with θ, the values of $\partial x/\partial\zeta$, $\partial x/\partial t$, and $\partial^2 x/\partial\zeta\,\partial t$ can be calculated. By this construction x and y are continuously known in the poloidal plane.

A big advantage of the isoparametric mapping is that during the iteration of the nonlinear equation (B.4) the grid of finite elements can be adjusted to the nonconverged solution obtained so far. Adjusting the positions of the elements, such that in the converged solution the nodal points coincide with flux surfaces, features the mapping from the cylindrical R, ϕ, Z system into flux coordinates s, χ, ϕ. From Eq. (B3.b) it is straightforward to evaluate R = R(s, χ) and Z = Z(s, χ). In this fashion we construct numerically from Eq. (B.3b) using a 4-point Gaussian quadrature integration along each element boundary the corresponding derivatives for χ, i.e.

$$\chi_{\zeta 0,t0}, \quad \frac{\partial\chi_{\zeta 0,t0}}{\partial\zeta}, \quad \frac{\partial\chi_{\zeta 0,t0}}{\partial t}, \quad \frac{\partial^2\chi_{\zeta 0,t0}}{\partial\zeta\,\partial t}.$$

The determinant of the transformation is given by

$$J = \frac{\partial x}{\partial\zeta}\frac{\partial y}{\partial t} - \frac{\partial y}{\partial\zeta}\frac{\partial x}{\partial t}. \tag{B.11}$$

Then the derivatives yield

$$\begin{pmatrix} \frac{\partial\psi}{\partial x} \\ \frac{\partial\psi}{\partial y} \end{pmatrix} = \frac{1}{J}\begin{pmatrix} \frac{\partial y}{\partial t} & -\frac{\partial y}{\partial\zeta} \\ -\frac{\partial x}{\partial t} & \frac{\partial x}{\partial\zeta} \end{pmatrix}\begin{pmatrix} \frac{\partial\psi}{\partial\zeta} \\ \frac{\partial\psi}{\partial t} \end{pmatrix} \tag{B.12}$$

and correspondingly for $(\partial\chi/\partial x, \partial\chi/\partial y)^{\mathrm{T}}$. Note that the converged solution satisfies along a flux contour $\partial\psi/\partial t = 0$. Then we get

$$|\nabla\psi|^2 = \left(\frac{\partial\psi}{\partial\zeta}\right)^2\left[\left(\frac{\partial x}{\partial t}\right)^2 + \left(\frac{\partial y}{\partial t}\right)^2\right]\Big/J^2. \tag{B.13}$$

Thus

$$g^{11} = 1/f^2|\nabla\psi|^2. \tag{B.14}$$

Eventually the quantity $\nabla\psi \cdot \nabla\chi$ is given by

$$\nabla\psi \cdot \nabla\chi = \left\{\frac{\partial\psi}{\partial\zeta}\frac{\partial\chi}{\partial\zeta}\left[\left(\frac{\partial x}{\partial t}\right)^2 + \left(\frac{\partial y}{\partial t}\right)^2\right] - \frac{\partial\psi}{\partial\zeta}\frac{\partial\chi}{\partial t}\left[\frac{\partial x}{\partial\zeta}\frac{\partial x}{\partial t} + \frac{\partial y}{\partial\zeta}\frac{\partial y}{\partial t}\right]\right\}\Big/J^2, \tag{B.15}$$

and furthermore,

$$g^{12} = 1/f\nabla\psi \cdot \nabla\chi, \tag{B.16}$$

$$g_{33} = 1/g^{33} = R^2, \tag{B.17}$$

$$g^{22} = \frac{1}{g^{11}}[R^2/J^2 + (g^{12})^2]. \tag{B.18}$$

All quantities which depend only on the radial coordinate s are represented by cubic splines. This allows accurate evaluation at all points required in the s integration based on 4-point Gaussian quadratures. Functions which depend both on the radius and on the poloidal angle χ are represented by a Fourier–cubic spline interpolation as introduced in (A.1). This interpolation is applied to the following 16 equilibrium quantities:

$$R^2; \qquad\qquad \frac{\partial}{\partial s}R^2; \qquad\qquad R^4$$

$$|\nabla\psi|^2; \qquad\qquad \frac{s^2}{|\nabla\psi|^2}; \qquad\qquad \frac{\partial}{\partial s}|\nabla\psi|^2$$

$$R^2|\nabla\psi|^2; \qquad R^4|\nabla\psi|^2; \qquad \frac{s^2R^2}{|\nabla\psi|^2}; \qquad\qquad \frac{s^2}{R^2|\nabla\psi|^2}$$

$$\nabla\psi\cdot\nabla\chi; \qquad R^2\nabla\psi\cdot\nabla\chi; \qquad R^4\nabla\psi\cdot\nabla\chi$$

$$\frac{s^2(\nabla\psi\cdot\nabla\chi)^2}{|\nabla\psi|^2}; \qquad \frac{s^2R^2(\nabla\psi\cdot\nabla\chi)^2}{|\nabla\psi|^2}; \qquad \frac{s^2R^4(\nabla\psi\cdot\nabla\chi)^2}{|\nabla\psi|^2}.$$

APPENDIX C: DETAILS OF THE FINITE ELEMENTS

Two orthogonal functions define a complete set of finite elements. The cubic Hermitian elements read (Ref. [26])

$$H_j(s) = \begin{cases} 3\left(\frac{s-s_{j-1}}{s_j-s_{j-1}}\right)^2 - 2\left(\frac{s-s_{j-1}}{s_j-s_{j-1}}\right)^3, & s_{j-1}\le s\le s_j, \\[2mm] 3\left(\frac{s_{j+1}-s}{s_{j+1}-s_j}\right)^2 - 2\left(\frac{s_{j+1}-s}{s_{j+1}-s_j}\right)^3, & s_j\le s\le s_{j+1}, \\[2mm] 0, & s\notin[s_{j-1}, s_{j+1}], \end{cases} \tag{C.1a}$$

$$\hat{H}_j(s) = \begin{cases} (s-s_j)\left(\frac{s-s_{j-1}}{s_j-s_{j-1}}\right)^2, & s_{j-1}\le s\le s_j, \\[2mm] (s-s_j)\left(\frac{s-s_{j+1}}{s_{j+1}-s_j}\right)^2, & s_j\le s\le s_{j+1}, \\[2mm] 0, & s\notin[s_{j-1}, s_{j+1}], \end{cases} \tag{C.1b}$$

and the quadratic elements

$$h_j(s) = \begin{cases} 2\left(s-\frac{s_j+s_{j-1}}{2}\right)\frac{(s-s_{j-1})}{(s_j-s_{j-1})^2}, & s_{j-1}\le s\le s_j, \\[2mm] 2\left(s-\frac{s_{j+1}+s_j}{2}\right)\frac{(s-s_{j+1})}{(s_{j+1}-s_j)^2}, & s_j\le s\le s_{j+1}, \\[2mm] 0, & s\notin[s_{j-1}, s_{j+1}], \end{cases} \tag{C.1c}$$

$$\hat{h}_j(s) = \begin{cases} 4\frac{(s-s_{j-1})(s_j-s)}{(s_j-s_{j-1})^2}, & s_{j-1}\le s\le s_j, \\[2mm] 0, & s\notin[s_{j-1}, s_j]. \end{cases} \tag{C.1d}$$

The elements are plotted in Fig. 2. Since every finite element extends over two radial intervals a block–tridiagonal structure is induced in the **A** and **B** matrices in Eq. (3.25). This

FIG. 10. (a) Block–tridiagonal structure of the **A** (and **B**) matrix with dimension $N = 16 \times M \times N_S$ ($N_S + 1 =$ number of radial points). (b) Bilinear interaction between the two orthogonal cubic finite elements per interval. The size of the blocks ZMA is $N_{ZMA} = 2 \times 8 \times M$ ($M =$ number of poloidal Fourier harmonics).

block–tridiagonal form is displayed in Fig. 10, where the interaction between element j and element $j + 1$ is highlighted as subblock ZMA. The χ-integration is performed by means of Fourier transforms as described in Eqs. (A.1–A.2). In addition, the 2×2 substructure due to the two orthogonal finite elements in every radial interval is shown in Fig. 10 for the eight variables. This completes the description of the matrices for the eigen problem.

REFERENCES

1. W. Kerner, *J. Comput. Phys.* **85**, 1 (1989).

2. W. Kerner, in *Large-Scale Eigenvalue Problems, Proceedings, IBM Europe Inst. Workshop on Large Scale Eigenvalue Problems, Oberlech, Austria, July 8–12, 1985* (North-Holland, Amsterdam, 1986), p. 241.

3. W. Kerner, K. Lerbinger, R. Gruber, and T. Tsunematsu, *Comput. Phys. Commun.* **36**, 225 (1985).

4. R. Gruber, F. Troyon, D. Berger, L. C. Bernard, S. Rousset, R. Schreiber, W. Kerner, W. Schneider, and K. V. Roberts, *Comput. Phys. Comm.* **21**, 323 (1981).

5. R. C. Grimm, J. M. Greene, and J. L. Johnson, *Methods Comput. Phys.* **16**, 253 (1976).

6. R. Gruber and F. Rappaz, in *Finite-Element Methods in Linear Ideal MHD* (Springer-Verlag, Berlin, 1985).

7. D. Borba, K. S. Riedel, W. Kerner, G. T. A. Huysmans, and M. Ottaviani, *Phys. Plasma* **1**, 3151 (1994).

8. W. Kerner, K. Lerbinger, and J. Steuerwald, *J. Comput. Phys. Commun.* **38**, 27 (1985).

9. M. S. Chance, J. M. Greene, R. C. Grimm, J. L. Johnson, J. Manikham, W. Kerner, D. Berger, L. C. Bernard, R. Gruber, and F. Troyon, *J. Comput. Phys.* **28**, 1 (1978).

10. C. Z. Cheng and M. S. Chance, *J. Comput. Phys.* **71**, 124 (1987).

11. A. R. Schellhase and R. G. Storer, *J. Comput. Phys.* **123**, 15 (1996).

12. L. S. Solovev, *Zh. Eksp. Teor. Fiz.* **53**, 626 (1967); *Sov. Phys.-JETP* **26**, 400 (1968).

13. W. A. Cooper, G. Y. Fu, R. Gruber, C. Schwab, U. Schwenn, S. Merazzi, and D. V. Anderson, in *Plasma Physics and Controlled Nuclear Fusion Research, 1990* (IAEA, Vienna, 1991), Vol. 2, p. 193.

14. A. Bondeson, G. Vlad, and H. Lütjens, in *Controlled Fusion and Plasma Heating, Proceedings of the 17th European Conference, Amsterdam, The Netherlands* (European Physical Society, Petit-Lancy, 1990), Vol. 14B, Part II, p. 906.

15. G. Y. Fu, W. A. Cooper, R. Gruber, U. Schwenn, and D. V. Anderson, in *Phys. Fluids B* **4**, 1401 (1992).

16. A. Bondeson and G. Y. Fu, in *Comput. Phys. Commun.* **66**, 167 (1991).

17. M. N. Busssac, R. Pellat, D. Edery, and J. L. Soule, *Phys. Rev. Lett.* **35**, 1638 (1975).

18. A. B. Mikhailovskii, in *Rev. Plasma Physics*, edited by M. A. Leontovich (Consultants Bureau, New York, 1986), Vol. 9, p. 1.

19. R. J. Hastie, T. C. Hender, B. A. Carreras, L. A. Charlton, and J. A. Holmes, *Phys. Fluids* **30**, 1756 (1987).

20. G. T. A. Huysmans, J. P. Goedbloed, and W. Kerner, *Phys. Fluids B* **5** (5), 1545 (1993).

21. A. Bondeson, G. Vlad, and H. Lütjens, *Phys. Fluids B* **4** (7), 1889 (1992).

22. C. Z. Cheng and M. S. Chance, *Phys. Fluids* **29**, 3695 (1986).

23. A. Fasoli, J. B. Lister, S. E. Sharapov, S. Ali-Arshad, G. Bosia, D. Borba, D. J. Campbell, N. Deliyanakis, J. A. Dobbing, C. Gormezano, H. A. Holties, G. T. A. Huysmans, J. Jacquinot, A. Jaun, W. Kerner, P. Lavanchy, J.-M. Moret, L. Porte, A. Santagiustina, and L. Villard, *Nucl. Fusion* **35**, 1485 (1995).

24. A. De Ploey, R. A. M. Van der Linden, G. T. A. Huysmans, M. Goossens, W. Kerner, and J. P. Goedbloed, *Plasma Phys. Control. Fusion* **39**, 423 (1997).

25. G. T. A. Huysmans, J. P. Goedbloed, and W. Kerner, *Proc. CP90 Conf. on Comp. Phys. Proc.* (World Scientific Publ. Co. 1991), p. 371.

26. O. C. Zienkiewicz, *The Finite Element Method in Engineering Science* (McGraw–Hill, London, 1971).